Supplementary Method 1: Estimating the frequency-dependent viscoelastic modulus, G*(ω), in SHEAR

We have previously detailed methods to estimate the spatially-averaged frequency-dependent shear modulus, G*(ω), from time-varying speckle patterns (25-30). Briefly, the speckle intensity auto-correlation curve, $g_2(t)$, was evaluated by measuring the correlation between pixel intensities in the first speckle frame (time point t_0) and subsequent frames. Spatial averaging was performed over all the pixel in the frame and several $g_2(t)$ curves, evolving in time, were averaged to improve the statistical accuracy, as follows:

$$g_2(t) = \langle \frac{\langle I(x,y,t+t_0) I(x,y,t_0) \rangle_{x,y}}{\langle I(x,y,t_0) \rangle_{x,y}^2} \rangle_{t_0} \quad (1)$$

Where $I(x,y,t+t_0)$ and $I(x,y,t_0)$ refer to the intensity values at pixel (x,y) and at times $t+t_0$ and t_0. Moreover, $< >_{x,y}$ indicates spatial averaging over all the pixels, and $< >_{t0}$ indicates temporal averaging. From the $g_2(t)$ curve, the spatially-averaged mean square displacements (MSD) of scattering particles is deduced via:

$$g_2(t) = 1 + e^{-2\gamma\sqrt{k^2\langle \Delta r^2(t) \rangle}} \quad (2)$$

Here, $k=2\pi n/\lambda$ is the wave number, n is the refractive index, λ is the wavelength, and $<\Delta r^2(t)>$ is the MSD. In addition, γ is an experimental parameter that depends on the relative proportions of long diffuse paths and short non-diffusive ones, and systematically varies with the polarization state of the received light and the scattering particle size (25,26,52). Previous experimental studies by other groups have tabulated the γ as a function of polarization state and scattering particle size. For cross-polarized speckle acquisition, as the scattering particles' radius, a, increases from 50 nm to 500 nm, γ decreases from 3.1 to 2.1. For the scattering particles' radius of a~100 nm, γ = 2.5(52). Substituting the MSD in the generalized Stokes-Einstein relation (GSER) yields the complex shear viscoelastic modulus as follows:

$$G^*(\omega) = \frac{K_B T}{\pi a i \omega \mathcal{F}\{\langle \Delta r^2(t) \rangle\}} \quad (3)$$

Here, K_B =1.38064852 × 10^{-23} is the Boltzmann constant, T is the temperature in Kelvins, $\mathcal{F}$ is Fourier transform, a is the scattering particle radius, and ω is the angular frequency in rad/s. Since in practice the temporal resolution and range of MSD is limited, direct calculation of the Fourier transform in the GSER can lead to truncation errors at the frequency limits(31,32).Instead, an algebraic approximation is used, based on fitting the MSD to a power-law form, i.e. $\langle \Delta r^2(t) \rangle \propto t^{\alpha}$, where $\alpha(t) = \left| \frac{\partial \ln (\langle \Delta r^2(t) \rangle)}{\partial \ln (t)} \right|$ is the log-log slope of MSD (31). This permits writing:

$$|G^*(\omega)| = \left. \frac{K_b T}{a\pi\Gamma(\alpha(\frac{1}{\omega}))+1)\langle \Delta r^2(1/\omega) \rangle} \right|_{\omega=1/t} \quad (4)$$

where Γ is the gamma function and α is evaluated at t=1/ω. Subsequently, the elastic (storage) and viscous (loss) moduli may be evaluated from the |G*(ω)| and α(1/ω) as:

$$G'(\omega) = |G^*(\omega)| \times \cos\left(\frac{\pi}{2}\alpha(1/\omega)\right),$$

$$G''(\omega) = |G^*(\omega)| \times \sin\left(\frac{\pi}{2}\alpha(1/\omega)\right). \quad (5)$$

Because the approximation assumes symmetry between time dependent MSD at time t and the frequency-dependent G* at ω=1/t rad/s, the SHEAR frequency range is determined by the frame rate, F_s, of the CMOS detector and imaging duration, T, according to $1/T<\omega<F_s$ (31,53).

For the breast tissue specimens, the speckle frame series were acquired at 250 fps (fps), for 1 second, corresponding to frequency range of ω: 1-250 rad/s, which is sufficient for the purpose of comparing and validating SHEAR against mechanical rheometry that is restricted to measurements at lower angular frequencies. A substantially larger range of frequencies can be accessed by operating the current camera, Basler acA2000-340km at higher frame rate of 6000 fps to extend

the frequency range up to 6000 rad/s.

Supplementary Fig. S1(A) displays the $g_2(t)$ curves for a soft polyacrylamide gel (Acrylamide 3%, bis-acrylamide 1%) and a stiff polyethylene glycol diacrylate gel (PEG 15%), obtained by cross-correlation analysis of speckle frames, acquired from a field of view of 20x20 mm^2, over T=4 seconds. The corresponding |G*(ω)| values measured using a standard rheometer at ω=10π (5 Hz) for the soft and stiff gels were 0.071 kPa and 70.34 kPa, respectively. The MSD of particles extracted from the $g_2(t)$ curves indicate that the particles exhibit larger displacements in the soft PA gels compared to the stiffer PEG gel (Supplementary Fig. S1(B)).

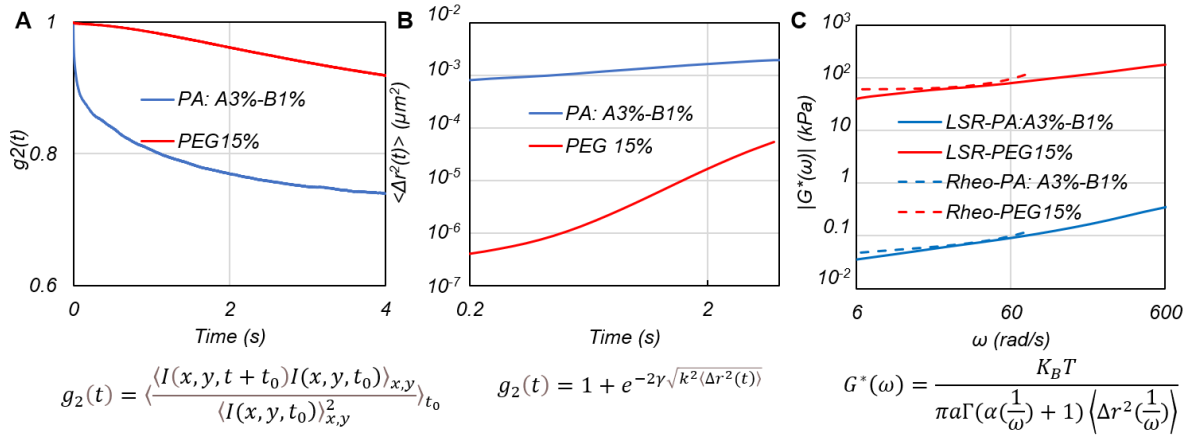

Supplementary Figure S1. Shear moduli measured in a soft polyacrylamide gel and a stiff polyethene glycol gel from laser speckle patterns. (A) Speckle intensity autocorrelation curves, $g_2(t)$, measured for a soft Polyacrylamide (PA, Acrylamide 3%-Bis-acrylamide 1%) vs a stiff polyethylene glycol diacrylate (PEG) 15%, measured over 20x20 mm^2 RoI over 4 seconds. (B) Mean square displacements of particles are deduced from $g_2(t)$. (C) The |G*(ω)| curves obtained via the GSER (solid) and from the rheometer (dotted). Close correspondence is observed between the two measurements for both the soft and stiff gel. For instance, at ω=10π rad/s: SHEAR |G*| = 0.067 kPa) for the soft PA gel and SHEAR |G*| = 66.5 kPa for the stiffer PEG gel. The shear moduli measured using a rheometer at the same frequency were 0.071 kPa and 70.34 kPa, respectively.

Supplementary Fig. S1(C) depicts the |G*(ω)| curves obtained via eqn. 1 (solid lines). For these gels, speckle frames were acquired at 600 fps, yielding an upper frequency limit of 600 rad/s. These curves closely agree with the rheometer measurements, confirming that the viscoelastic properties of stiffer samples may be probed by acquiring time-varying speckle frames that evolve

over time. Because in SHEAR light is multiply scattered from particles, even minute motions (fraction of a wavelength, in the order of few nm) of particles, encountered within each light path, give rise to cumulative optical phase shifts that induce perceptible speckle intensity fluctuations. As a result, the minimum perceptible displacement of individual particles that could induce a phase shift of π, and an appreciable speckle intensity change is much smaller than λ. Given that λ=633 nm, in theory the smallest displacements that SHEAR can resolve are in the order of tens of nm. Therefore, SHEAR can characterize much stiffer samples compared to standard DLS, because only very small particle displacements are required to probe the viscoelastic properties of the material.

Supplementary Method 2: Estimating the scattering particle size

To evaluate $|G^*(\omega)|$ via eqn. 4 in SHEAR the average size of scattering particles, *a*, needs to be estimated. We estimated the *a* from speckle fluctuation rates at perpendicular and parallel polarizations, based on the following concept. When the sample is illuminated by a linearly polarized beam, the parallel-polarized component of remitted speckle fluctuates slower than the perpendicularly polarized one, as seen in the $g_{2\perp}(t)$ and $g_{2\parallel}(t)$ curves of normal adipose and fibrous, and invasive carcinoma breast tissue in Fig. S2(A-C). This is intuitively explained by noting that the parallel polarized component of the back-scattered light contains a relatively larger proportion of shorter optical paths that have scattered only once. The number of short optical trajectories increases as the scattering particles become smaller. This is because for smaller particles the scattering is isotropic rather than forwardly directed and the single-scattered photons are more likely to return towards the detector.

To investigate this trend, we used a polarized correlation transfer Monte-Carlo Ray Tracing (MCRT), to simulate the speckle intensity autocorrelation curves, $g_2(t)$ at parallel and perpendicular states, for media of different scattering particle sizes. The refractive indices of air,

nv=1, tissue microenvironment, n_t=1.36, and scattering particles n_{sp}=1.59 were chosen based on previously published values (54). For each scattering particle size, the concentration was adjusted such that the reduced scattering coefficient, μ_s', is maintained at 1 mm^{-1}, which is in the order of values reported in the literature for breast tissue (55).

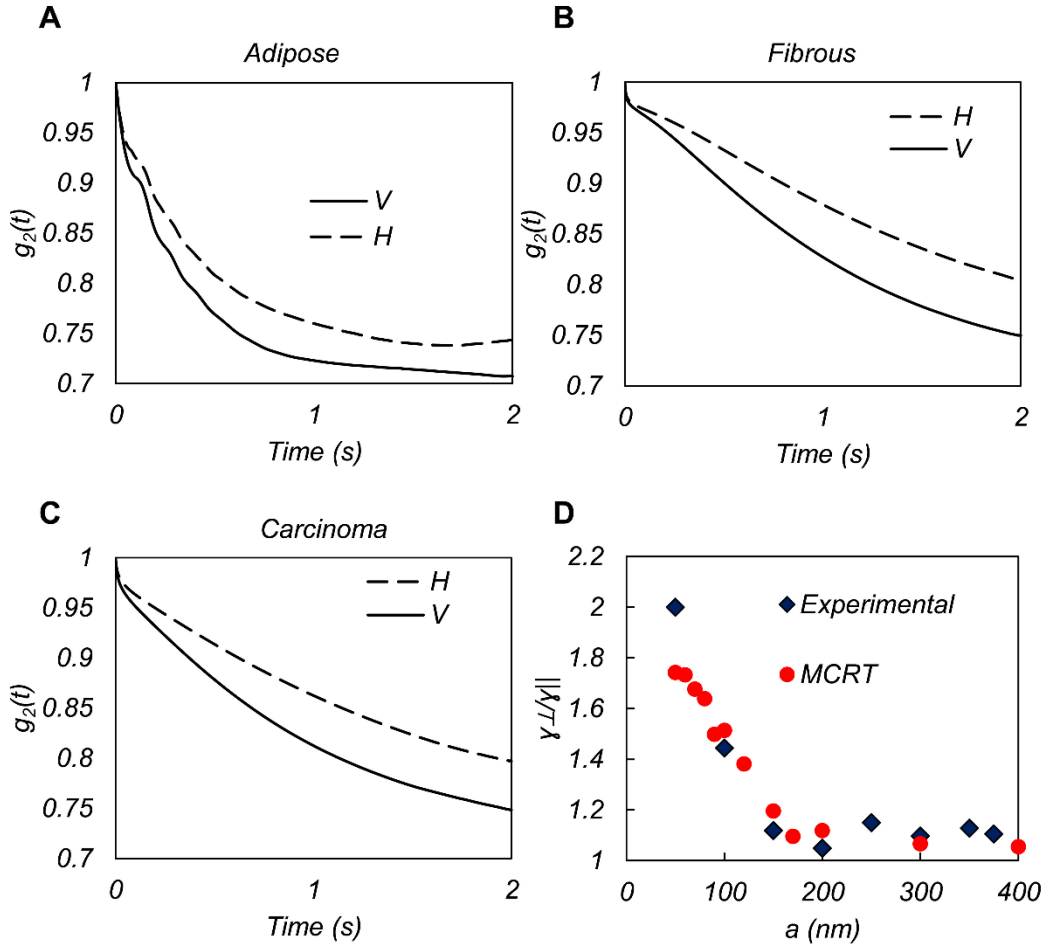

Supplementary Figure S2. Representative $g_{2\perp}(t)$ and $g_{2\parallel}(t)$ curves, and the calibration curve displaying $\gamma_\perp/\gamma_\parallel$ vs *a*. (A) Normal adipose, (B) Normal fibrous, and (C) Carcinoma specimens. (D) MCRT simulations and experimental results, displaying the ratio of log($g_2(t)$), i.e. $\gamma_\perp/\gamma_\parallel$vs scattering particle size, demonstrating that the scattering particles may be estimated from the ratio of the log of $g_2(t)$ curves at perpendicular and parallel polarization states obtained experimentally. For these representative curves we obtain adipose, $\gamma_\perp/\gamma_\parallel$=1.32, a=120 nm, (B) fibrous, $\gamma_\perp/\gamma_\parallel$=1.5, a=100 nm, (C) invasive ductal carcinoma (IDC), $\gamma_\perp/\gamma_\parallel$=1.43, a=110 nm.

The photon trajectories were tracked and the $g_2(t)$ curves were simulated as:

$$g_2^{MCRT} - 1 = \left(\int_0^{\omega} P(Y) e^{-\frac{1}{3}k^2\langle\Delta r^2(t)\rangle Y} dY\right)^2 \quad (6)$$

Here, $Y=\sum q^2/(2k_0^2)$, is the cumulative momentum transfer, $q=2k_0\sin(\theta/2)$ is the momentum transfer at the individual scattering events, and P(Y) is the probability distribution of momentum transfer for each polarization state, obtained by tracking the Stokes vector components [I, Q, U, V], at each scattering event and multiplying it with the Stokes vector of the polarizer in the detection arm. The simulation model provided the $g_2(t)$ curves at parallel, $g_{2||}(t)$, and perpendicular, $g_{2\perp}(t)$ polarizations. Subsequently, the following ratio was calculated

$$\frac{\log\left(g_{2\perp}(t)-1\right)}{\log\left(g_{2||}(t)-1\right)}=\frac{\gamma_{\perp}}{\gamma_{||}}. \tag{7}$$

where $g_2(t)-1=e^{-2\gamma\sqrt{k^2\langle\Delta r^2(t)\rangle}}$. Nevertheless, due to the numerical nature of simulations, the left side of eqn. 7 could vary with time. Therefore, the ratio was evaluated at a time point where there was the largest separation between $g_{2\perp}(t)$ and $g_{2||}(t)$. Tabulating the scattering particle size, *a*, vs the simulated $\frac{\gamma_{\perp}}{\gamma_{\parallel}}$, permitted retrieving the average particle size from the experimentally evaluated $g_{2\perp}(t)$ and $g_{2||}(t)$ (Fig. S2(D)). Alternatively, $g_2(t)$-1 can be fitted to a model function $y=e^{-2\gamma\sqrt{k^2x}}$ to estimate the multiplicative factor in the exponent and directly evaluate the $\gamma_{\perp}$ and $\gamma_{||}$. For the representative curves in the supplementary Fig. S2, the result of this analysis was as follows:

Adipose, $\gamma_{\perp}/\gamma_{||}$=1.32, a=120 nm,

Fibrous, $\gamma_{\perp}/\gamma_{||}$=1.5, a=100 nm,

Carcinoma, $\gamma_{\perp}/\gamma_{||}$=1.43, a=110 nm.

We further expanded the analysis to a larger representative set of 23 breast tissue samples to investigate the variations in *a*. The median value of estimated *a* was 85 nm for normal fibroadipose breast tissue (N=14) and 135 nm for carcinoma (N=9). Over all 23 breast tissue samples, we estimated the median particle size was 105 nm, with an interquartile range (IQR) of approximately

±35 nm.

This method is primarily sensitive to *a* in the sub-micron range. We have previously developed another approach for estimating the *a* from the specific spatial pattern of the time averaged speckle frames in parallel polarization state (27). This pattern evolves from a bi-lobular pattern for scattering particle size of *a*=100 nm to a clover-like quadrilateral shape for *a=3 μm*, and enables estimating larger particle sizes in the 0.1-3 μm range. Combining these two approaches may enable particle sizing over an extended range in the future.

The methods described above are based on the fact that in SHEAR, the scattering signal projected on each pixel is scattered multiple times along the probed depth before impinging on the detector. Therefore, the ensemble of scattering events from randomly-oriented small-sized particles converges with that obtained from an ensemble of volume-equivalent spherical particles (56). For non-spherical particles within the tissue, this corresponds to the average sphere-equivalent hydrodynamic radius, *a*, parameter that needs to be replaced in the GSER to evaluate the $G^*(\omega)$(57).

Supplementary Method 3: Characterizing the spatial resolution of the SHEAR

In the current manuscript, we provided an estimated spatial resolution of 50 μm for the SHEAR method. This is based on experimental evidence on the sizes of the smallest structural features that were distinguished by this technology.

Theoretically, the spatial resolution of the SHEAR is derived, based on the followings:

1. Optical diffraction limit: In principle, the resolution of $|G^*(x,y)|$ maps may not exceed the resolution of imaging optics. In the current optical setup, we have used an objective lens of 10x (NA = 0.25). At a source wavelength of λ=632 nm, this objective sets the diffraction

limit, i.e. airy disk size or speckle grain size, (1.22λ/(2×NA)) to 1.5 μm, in the object plane (58). This corresponds to a spot size of 1.5×10x=15 μm at the camera sensor. The speckle size and resultant spatial resolution of SHEAR can be improved by using objective lenses of higher NA and magnification.

2. Spatial and temporal contrast of the speckle pattern grains: Sufficient spatial and temporal contrast is needed to avoid blurring of the speckle grains, which could reduce the spatial resolution and contrast of |G*(x,y)| maps. To overcome this issue, speckle patterns should be fully developed in both space and time, with the intensity levels spanning the full pixel depth of the CMOS. The high-speed Basler camera in the SHEAR setup has 2046 × 1086 pixels, 5.5 μm pixel size, and is operated at 8-bit pixel depth (intensity levels: 0-255). Given the speckle spot size of 15 μm in the image plane, a pixel to speckle ratio of ~3×3=9 is obtained, which ensures sufficient spatial speckle contrast. Moreover, the camera frame rate also influences the overall spatial resolution given its influence on speckle contrast. Using the high frame rate acquisition capability of the CMOS, operated at 250 fps in the current study, permits sufficient temporal sampling of speckle fluctuations and enables tracking the rapid dynamics of the speckle patterns, thus reducing the influence of speckle blurring.
3. The amount of spatial and temporal averaging: In SHEAR ensemble averaging of temporally fluctuating speckle spots is required to calculate the MSD with sufficient statistical accuracy. This can be achieved by using a combination of spatial and temporal averaging of fluctuating speckle patterns. Combined spatio-temporal averaging may be accomplished by sliding a moving-average spatial Gaussian window across the pixels of the speckle patterns and by time-averaging multiple $g_2(t)$ curves that evolve in time. This

permits shorter acquisition times albeit at the cost of a reduced spatial resolution of the |G*(x,y)| map. In the SHEAR processing scheme, a 16x16 Gaussian window with a standard deviation of 4 pixels reduces the theoretical resolution to 24 μm. The spatial resolution may be improved by exploiting a smaller moving average window but at the expense of acquiring speckle images for longer times to compensate and trade the reduced spatial averaging with increased temporal averaging of multiple $g_2(t)$ curves that evolve in time.

4. The influence of multiple scattering and light diffusion on the resolution and sensitivity: Since in SHEAR the detected light is scattered multiple times, significant speckle intensity fluctuations occur among scattering centers located at sub-resolution distances from each other, yielding acute sensitivity to sub-diffraction limited changes in the Brownian displacements and viscoelastic susceptibility of the microenvironment(52). However, intensity fluctuations of individual speckle grains reflect the average Brownian dynamics of the entire sampling volume, determine by the numerical aperture (NA) of the objective. Therefore, multiply scattered light from neighboring regions may still end up within the sampling volume and reduce the contrast and resolution of the SHEAR maps.

For the same reasons, in its current form, SHEAR provides depth-integrated measurements and does not bear depth-sectioning capability. In the current study we used a 10x objective with NA of 0.25. This corresponds to an imaging depth of 800 μm for a full field of view (FoV) of 1600 μm. Nevertheless, the camera sensor imaged a reduced FoV of 500×500 μm^2, which corresponds to an imaging depth of 250 μm. In our histology comparisons, we acquired the H&E sections of the tissue across multiple depths through the entirety of the sample, with 100 μm spacing between the sections, and a 7μm thick tissue section per slide. The |G*(x,y)| maps

showed the closest resemblance to the sections at 100-400 μm beneath the surface.

Supplementary Method 4: Quantifying micro-mechanical heterogeneities:

We estimated the heterogeneity of $|G^*(x,y)|$ within tumor samples using three metrics. Firstly, we estimated distinct variations in $|G^*(x,y)|$ between the tumor epithelium and stroma by segmenting these regions. Secondly, we evaluated the gradient of $|G^*(x,y)|$, i.e. $|\nabla|G^*(x,y)||$ at the epithelium and stroma interface, termed the invasive front (IF). Thirdly, we estimated a metric of statistical variations characterized by information entropy of $|G^*(x,y)|$ maps.

The calculations of the first two metrics were guided by the co-registered H&E image to segment out the $|G^*(x,y)|$ map into tumor epithelium and stroma and to delineate the invasive front (IF). In our study, 58 out of 111 tumors clearly showed both stromal and epithelial compartments within the same H&E slides and were analyzed as follows. Each H&E image was transferred from the RGB (i.e. Red/Blue, Green) to Lab color space. The Lab color space assigns three variables to each pixel, namely luminosity, L, chromaticity a*, indicating where color falls in the red-green axis, and chromaticity 'b*' indicating where the color is along the blue-yellow axis. The H&E image pixels were clustered based on their a* and b* values. Conceptually, the clustering was performed by finding the borderlines along the a* and b* plane, such that the image pixels corresponding to each cluster were closest to each other and farthest from objects in other clusters. In simple words, the stromal and epithelial component were segmented out in the H&E section, based on their distinct pink and blue shades. Supplementary Fig. S3 (A, B) displays the pixels of the digitized H&E slide that correspond to the tumor stroma and epithelium for an IDC tumor specimen. These clusters of pixels were used to create spatial masks to separate out the tumor from the stroma. Averaging the $|G^*(x,y,\omega)|$ values at $\omega = 2\pi$ rad/s for all the pixels within the tumor

epithelium and stroma returned the $\overline{|G^*|}$ of these components.

To evaluate the gradient metric in the |∇|G*(x,y)|| maps, we applied the gradient function in MATLAB®. This gradient operator returns a 2-dimensional vector for each pixel within the |G*(x,y)| matrix, at ω=2π rad/s. The x and y components of this vector effectively corresponding to the finite differences between the adjacent pixel values in the horizontal and vertical directions. The notation, |∇|G*(x,y)|| refers to the total magnitude of this gradient vector. Due to the numerical nature of the MATLAB gradient function, speckle noise and local heterogeneities between a few adjacent pixels could induce artefacts in the |∇|G*(x,y)||. Therefore, Gaussian filtering of 500 pixels window size was applied to the |G*(x,y)| map (evaluated at ω=2π rad/s). Subsequently, the gradient function in MATLAB® was applied to the smoothed |G*(x,y)| maps. To evaluate the average gradient along the IF, i.e. $\overline{|\nabla|G^*||}$, the epithelium-stroma interface was manually traced on the segmented H&E image, as shown in Supplementary Fig. S3(A). Coordinates of the IF were automatically transformed to the co-registered |G*(x,y)| and |∇|G*(x,y)|| images (Supplementary Fig. S3 (C,D)). The trace was then fitted to a piecewise linear curve, with each segment being 400 μm long. The average |∇|G*(x,y)|| of the pixels along each segment of the trace, $\overline{|\nabla|G^*||}$, were calculated and recorded. Therefore, for each tumor fragment, a number N=L/400 μm of $\overline{|\nabla|G^*||}$ are reported, where L is the length of the invasive front borderline. This analysis was performed on 38 out of 111 tumor specimens, where the tumor and stroma could be clearly delineated in the same slide based on the H&E color segmentation.

The information entropy, H, was evaluated directly from the entire |G*(x,y)| map. To this end, the probability distribution function (PDF) of |G*(x,y,ω)| for each tumor was obtained at ω=2π rad/s (1 Hz). Subsequently, the information entropy was calculated as:

$$H(x) = -\sum_{i=1}^{n} P(|G^*|_i)\log\left(P(G^*|_i)\right) \quad (4)$$

Here, $P(|G^*|_i)$ is the probability that a pixel in the |G*(x,y)| map takes on the value of $|G^*|_i$. This analysis was performed on 106 out of 111 tumor specimens, for which the |G*(x,y)| maps were free of considerable mosaicking artefacts that artificially increased entropy values.

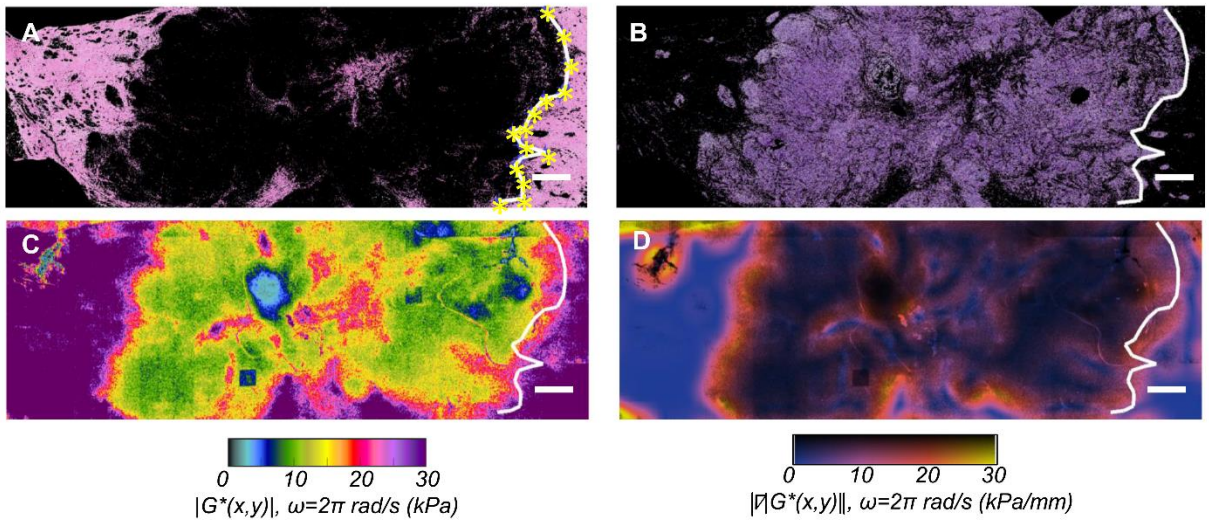

Supplementary Figure S3. The algorithm used to segment the |G*(x,y)| maps and delineate the invasive front. (A) The segmented tumor stroma obtained through color space analysis of the registered H&E slide. The invasive front (IF) is manually dotted along the boundary of the segmented stroma as shown by the yellow stars. A piece-wise linear fitted curve, displayed in white, is generated based on the dotted outline. (B) The segmented tumor epithelium and the piece-wise linear curve. The coordinates of the piece-wise linear IF curve are transferred to (C) the |G*(x,y)| map and (D) $|\nabla|G^*(x,y)||$, to evaluate the $\overline{|\nabla|G^*||}$ plotted in all the bar plots (Figs. 3-6) and Results in the main manuscript.

Supplementary Method 5: Comparison with conventional rheometry measurements:

We have previously shown the correspondence between a non-microscopic variant of SHEAR termed laser speckle rheology (LSR), that shares similar technological concepts of multi-speckle time-series acquisition over large fields of views (FoVs), with both rheometer and AFM. These included measurements in assorted agarose, polyethylene glycol diacrylate (PEG), and polyacrylamide (PA) hydrogel phantoms, exhibiting |G*(ω)|: *0-40 kPa*, ω=2π rad/s, as published in our prior papers (29). For these homogeneous phantoms, a strong and statistically significant

correlation was observed between the |G*(ω)| measured optically from laser speckle fluctuations and the rheometer (R=0.95, p<0.0001. Moreover, |G*(ω)| values measured by LSR were also significantly correlation with the AFM measurements of the indentation modulus , E (R=0.93, p<0.001) (29). The capability of the previous LSR technique for distinguishing heterogeneities was also confirmed by scanning the beam over the sample (29). In these prior results, we evaluated microfabricated composite Polydimethylsiloxane (PDMS)-PEG, composed of highly elastic PDMS bars (|G*(x,y)|=50 kPa) of different thicknesses (50-200 μm) , embedded within a soft PEG gel (|G*(x,y)|=0.3 kPa), which confirmed that mechanical heterogeneities could be resolved from the speckle intensity fluctuations (29).

The linear regression analysis of SHEAR vs conventional rheometer measurements in biological tissues, however, only returns a moderately strong correlation coefficient. This is likely because the conventional rheometry of tissue samples are challenging due to several experimental factors, including tissue dehydration, uneven contact area, variation in the normal force, and tissue slippage, among others. In the current study, A conventional strain-controlled rheometer (ARG2, TA instruments Inc., DE, USA) was used to evaluate the G*(ω) of breast tissue specimens. A parallel plate geometry was used with a top plate of 8 mm diameter. The experimental variations were minimized by implementing a protocol that minimizes the artifacts. These included using biopsy punches to cut the tissue to the cylinders of 8 mm dia. and height of 1.5 to ensure that the top plate is in contact with the entire tissue surface and that the tissue is deformed uniformly. Moisture traps were also used to prevent tissue dehydration. In addition, to maintain the grip and avoid sample slippage, particularly at higher frequencies, two pieces of sandpaper, cut to the size of the top and bottom plates, were secured to the rheometer plates. Moreover, the rheometer was calibrated prior to each set of experiments and rotational mapping of the top plate was performed

before the measurements to minimize the inertial effects as much as possible.

The regular normal force control approach, often used to adjust the rheometer gap size and properly sandwich the samples between the rheometer plates before applying the oscillatory shear stress while applicable to rubber-like elastic solids, could simply crush the squishy tissue samples. Instead, in the current study, the top plate was lowered in 100 µm steps until a small but significant change was observed in the normal force level, suggesting that the top plate has come into contact with tissue. Then the top plate was lowered by another 50 µm, to ensure proper sample contact. After conditioning, a frequency sweep oscillation procedure was performed, at the range of 0.628-250 rad/s, while maintaining the strain below 0.5%, to obtain the frequency-dependent G*(ω).

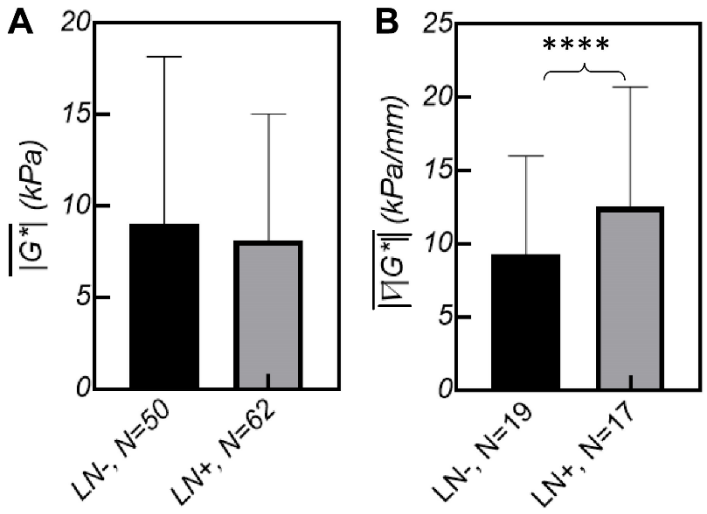

Supplementary Figure S4. Bar plots of (A) $\overline{|G^*|}$ of all tumors, and (B) $\overline{|\nabla|G^*||}$ in tumors with epithelial and stromal interface, excised from patients with lymph node (LN) negative (-) and positive (+) status. While $\overline{|G^*|}$ is not significantly different between these LN- and LN + groups, $\overline{|\nabla|G^*||}$ is significant higher at the invasive front of LN+ tumors. ($p<0.0001$: ****).

References:

1. Weitz DA, Pine DJ. Diffusing Wave Spectroscopy. In: Brown W, editor. Dynamic Light Scattering: The Method and Some Applications: Oxford University Press; 1993.
2. Maier T, Haraszti T. Python algorithms in particle tracking microrheology. **2012**
3. Schmitt JM, Kumar G. Turbulent nature of refractive-index variations in biological tissue. Opt Lett **1996**;21:1310-2
4. Chance B, Cooper CE, Delpy DT, Reynolds EOR, Tromberg BJ, Coquoz O, *et al*. Non-invasive measurements of breast tissue optical properties using frequency domain photon migration. Philosophical Transactions of the Royal Society of London Series B: Biological Sciences **1997**;352:661-8
5. Mishchenko MI, Travis LD, Lacis AA. Scattering, absorption, and emission of light by small particles. Cambridge ; New York: Cambridge University Press; 2002. xv, 445 p., 16 p. of plates p.
6. Pecora R. Dynamic Light Scattering Measuremt of nanometer partilces in liquids. Journal of Nanoparticle Research **2000**;2:123-31
7. Goodman JW. Speckle phenomena in optics : theory and applications. Second edition. ed. Bellingham: The International Society for Optical Engineering; 2020.

Supplementary TABLE S1. Multivariate analysis significance levels of prognostic criteria in association with $\overline{|G^*|}$.

Prognostic criteria	***p value***
Lesion size	0.392
Histological grade	0.002
Histological type	0.004
ER	0.791
PR	0.043
HER	0.861
Lymph node status	0.382

Supplementary TABLE S2. General Linear Model (GLM) parameters for the most important clinical determinants of $\overline{|G^*|}$.

	coefficient		95% Confidence interval		significance
Clinical parameter	**B**	**SE**	**Lower Bound**	**Upper Bound**	**p value**
Intercept	1.843	2.807	-3.725	7.410	.513
Histological type					
IDC	5.870	2.679	.557	11.184	.031
ILC	3.666	3.735	-3.742	11.073	.329
IDLC	7.531	3.114	1.354	13.707	.017
IMC	-4.428	5.116	-14.576	5.721	.389
IMPC	15.822	4.831	6.240	25.404	.001
IPC	0[a]	.	.	.	.
Histological grade					
Grade 1	8.946	2.626	3.737	14.154	.001
Grade 2	3.013	1.511	.016	6.010	.049
Grade 3	0[a]	.	.	.	.
PR status					
PR+	-3.406	1.660	-6.699	-.112	.043
PR-	0[a]	.			

Supplementary TABLE S3. Significance levels of prognostic criteria in association with $\overline{|\nabla|G^*||}$.

Prognostic criteria	***p value***
Lesion size	0.141
Histological grade	0.172
Histological type	<0.0001
ER	0.023
PR	0.110
HER	0.481
Lymph node status	0.047

Supplementary TABLE S4. Generalized Estimating Equation (GEE) parameters for $\overline{|\nabla|G^*||}$.

	coefficient		95% Wald confidence interval		significance
Clinical parameter	**B**	**SE**	**Lower Bound**	**Upper Bound**	**p value**
Intercept	15.3	6.6	2.47	28.2	.019
Histological type					
IDC	-8.7	4.7	-18	0.6	0.067
ILC	-16.6	4.5	-25.5	-7.7	.000
IDLC	-15.6	4.8	-25	-6.2	.001
IMC	-20.7	5.1	-30.7	-10.7	.000
IPC	-16.5	5.1	-26.6	-6.6	.001
IMPC	0a	.	.	.	.
LN status					
LN-	2.9	1.4	0.4	5.6	.047
LN+	0[a]	.	.	.	.
PR status					
ER-	-7.6	3.3	-14.2	-1	0.023
ER+	0[a]	.	.	.	.
PR status					
PR-	2.9	1.8	-0.66	6.4	.11
PR+	0[a]	.			
HER2 status					
HER2-	-2	2.8	-7.4	3.5	.481
HER2+	0[a]	.	.	.	.
Histological grade	1.3	0.93	-0.5	3	.172
Tumor size	.816	.5	-0.3	1.9	.141